coatings

MDPI

Article

Influence of Substrate Removal Method on the Properties of Free-Standing YSZ Coatings

Robert Vaßen *, Emine Bakan and Sigrid Schwartz-Lückge

Forschungszentrum Jülich GmbH, Institute of Energy and Climate Research IEK-1, 52425 Jülich, Germany; e.bakan@fz-juelich.de (E.B.); s.schwartz-lueckge@fz-juelich.de (S.S.-L.)
* Correspondence: r.vassen@fz-juelich.de

Abstract: Thermally sprayed ceramic coatings are often tested as free-standing layers to investigate different properties such as thermal expansion coefficient, thermal conductivity, sintering, mechanical behavior, corrosion resistance, gas tightness, or electrical properties. In this paper, four different substrate removal methods were used to obtain free-standing YSZ coatings. At first, spraying on a steel substrate and subsequent dissolution of the substrate-coating interface by hydrochloric acid (HCl) was used. Second, the steel substrate was removed by applying an electrical field via electrochemical corrosion of the surface of the substrate. In a third method, the coating was sprayed on a salt (NaCI) interlayer, which was removed later by dissolution in water. At last, the coating was sprayed on a graphite substrate and the substrate was removed by heat treatment. After the preparation of free-standing coatings, these were characterized using scanning electron microscopy, mercury porosimetry, indentation tests, and room temperature three-point bending tests, which allowed the determination of Young's modulus and viscosity. The results revealed measurable differences in coating properties as a result of the substrate removal methods, i.e., HCl method led to higher porosity and lower modulus in the YSZ coating.

Keywords: free-standing coatings; plasma spray; YSZ

Citation: Vaßen, R.; Bakan, E.; Schwartz-Lückge, S. Influence of Substrate Removal Method on the Properties of Free-Standing YSZ Coatings. *Coatings* **2021**, *11*, 449. https://doi.org/10.3390/coatings11040449

Received: 23 March 2021
Accepted: 11 April 2021
Published: 13 April 2021

1. Introduction

Thermally sprayed ceramic layers often have sufficient mechanical strength to be handled as free-standing coatings if they have a thickness in the range of 100 µm or above. Such free-standing coatings allow measurements of properties that are difficult or rather impossible to determine with a substrate underneath. These measurements can be mechanical tests, e.g., for the evaluation of Young´s modulus [1], bending strength [2], creep [3,4] or sintering properties [5–7], toughness [8], and crack propagation [9,10]. Additionally, functional properties like thermal diffusivity [11], optical properties [12], phase evolution [13], and attack by corrosive species as Calcium–Magnesium–Aluminum–Silicate (CMAS, [14]) are measured on free-standing coatings. The testing can be also possible with a substrate underneath, however, due to this additional component the evaluation process becomes more complex, and also the experimental error increases [15].

Thermal barrier coatings (TBCs) are used to reduce the surface temperature of metallic components in the hot section of gas turbine engines and thus to increase the operating temperature beyond the temperature capability of the metallic substrates. As temperature gradient testing of TBCs, i.e., heating the TBC surface while the substrate is cooled, is complex and expensive, isothermal testing of free-standing ceramic coatings at elevated temperatures is often the method of choice. Certainly, it should also be pointed out that the presence of a substrate also can affect the properties and hence the performance of the coating [16]. This is in many cases due to the residual stresses which

form in the coatings during manufacture or operation. The evolution of properties of coatings during operation may be influenced by the presence of the substrate as well. For instance, sintering is typically reduced in coatings on substrates as the shrinkage in two dimensions is constrained [17].

There are different possibilities for the preparation of free-standing coatings. In each method, it is imperative that the substrate removal process should not influence the coating property. For example, if an acid is used for dissolving the metallic substrate, it must be ensured that the ceramic coating does not react with that acid. In this paper, yttria-stabilized zirconia (YSZ) coatings will be considered and YSZ possesses rather high stability against acids. However, there have been certain indications that substrate removal by acids might still change the YSZ coating microstructure. For a more quantitative evaluation, four different substrate removal processes were used in the present study. Subsequently, the coatings were characterized using scanning electron microscopy (SEM), hardness tests, mercury porosimetry, and bending experiments. It should be mentioned here that a company is using the heating or cooling process for removal involving thermal stresses in the coated system [18]. This is due to the difference in thermal expansion coefficients and leads to a delamination. As it involves a certain heat-treatment, it is not considered here.

2. Materials and Methods

For the manufacture of the free-standing coatings, steel (40 × 30 × 2 mm^3) and graphite (25 × 25 × 5 mm^3) substrates were used using different removal methods. All substrates were coated simultaneously in the same atmospheric plasma spray (APS) deposition run using a TriplexPro torch (Oerlikon Metco, Switzerland), in a Multicoat spray facility. The YSZ starting powder used for the deposition (Metco 204 NS, Oerlikon Metco, Switzerland) had a particle size distribution (D10/D50/D90) of 21/53/95 μm. In the process, 46 standard liter pro minute (slpm) Ar and 4 slpm He plasma gas composition was used with a plasma current of 420 A and a stand-off distance of 200 mm. Total of 25 cycles were used to deposit coatings of about 600 μm thickness.

The removal methods are summarized in Table 1 and abbreviations noted for each method in this table will be used in the text hereinafter. Some further details of the removal methods are given in the following. In the NaCl method, prior to deposition of the YSZ layer, a 100 μm NaCl coating was applied by APS using the TriplexPro torch with a stand-off distance of 120 mm, a plasma current of 450 A, and 46/4 slpm Ar/He as process gas. The subsequently applied YSZ coating could be easily removed by dissolving the intermediate NaCl layer in water. It should be mentioned here that this method is not suitable for rather hot spraying conditions because in that case the coating might spall-off already during the deposition process. For the method EC, the steel substrates were emerged in a saturated solution of NaCl and then connected as the anode (positive) using another steel plate as the cathode. The applied voltage was about 4 V giving a current density of 2.2 A/cm^2. After several minutes the coating was removed from the substrate. In the HCl method, the coated substrate was soaked in 25% HCl acid to dissolve the substrate-coating interface and after about 14 h the coating was removed from the HCl acid. Possible reactions with the steel (major compound Fe) or the oxidized steel Fe_2O_3 are

$$Fe + 2\,HCL \rightarrow Fe^{2+} + 2\,Cl^{-} + H_2 \quad (1)$$

$$Fe_2O_3 + 6\,HCL \rightarrow 2\,Fe^{3+} + 6\,Cl^{-} + 3\,H_2O \quad (2)$$

Lastly, in the graphite method, the graphite substrate was burned in air (800 °C–5 h) following the deposition process. A photo of the YSZ free-standing coatings detached using these methods is shown in Figure 1. The brownish coloring of the coating in the NaCl and EC methods was associated with iron oxide coming from the steel substrates.

Table 1. Summary of the used substrate removal methods.

Abbreviation	Method
NaCl	Intermediate NaCl layer, removal by water
EC	Electrochemical removal applying voltage with a concentrated salt solution
HCl	Treatment in HCl for several hours
Graphite	Graphite substrate, subsequent heat-treatment in air

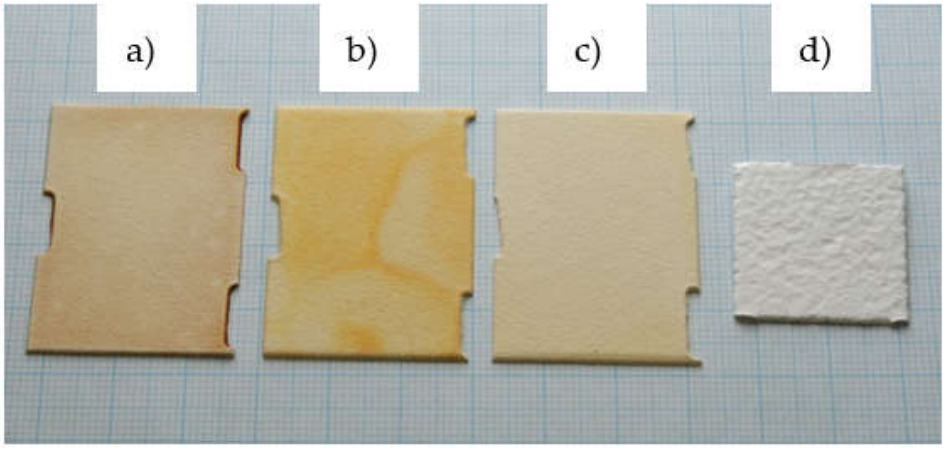

Figure 1. Photo of the YSZ free-standing coatings, from left to right the methods NaCl (**a**), EC (**b**), HCl (**c**), and graphite (**d**) were applied.

Metallographic cross sections were prepared from the free-standing coatings to investigate the microstructure using a SEM (Zeiss Ultra 55 FEG-SEM, Carl Zeiss Microscopy GmbH, Oberkochen, Germany). The pore size distribution was measured on the free-standing coatings by mercury (Hg) porosimetry using two units of porosimeters produced by CE Instruments, Italy (Pascal 140 for the low pressure and Pascal 440 for the high-pressure range). The size of the samples was 19 × 11 × 0.6 mm (≈125 mm^3), which is about the maximum dimensions of a sample of this thickness that can be measured in this facility. As the resolution of the mercury porosimetry is about 0.1 mm^3 and the expected pore volume is about 15%, this was expected to give a sufficient accuracy of the measurement.

The surface topography and roughness of the free-standing coatings were characterized by a non-contact profilometer using a confocal white light sensor with a vertical resolution of 0.035 μm (Cyber Scan, CT350T, Cyber Technologies, Munich, Germany). The thermo-mechanical analysis (TMA) of free-standing coatings was conducted by three-point bending test (Netzsch TMA 402 F1 Hyperion, Selb, Germany) at room temperature. Before the bending test, both sides of the coatings were ground with SiC paper to ensure uniform thickness. A maximum load (F) of 0.5 N was applied on 15 × 4.5 mm^2 sample size, while the loading-unloading displacement curve was simultaneously recorded. For the grip spacing of 10 mm, 5 MPa in-plane stress was estimated under the maximum load. Elastic modulus (E) of the coatings was calculated from the measured displacement (δ) during the unloading period:

$$E = \frac{F}{\lambda} \cdot \frac{1}{\Delta\delta_{unloading}} \quad (3)$$

$$\lambda = \frac{4bh^3}{L^3} \quad (4)$$

where b and h are sample width and thickness, respectively and L is grip spacing. The start and endpoints of the unloading period were determined using the second derivative of the time-displacement curve. The loading time under the constant maximum load was 10 min and the slope of the time-displacement curve within this period was used for the viscosity ($\eta, Pa.s$) calculation:

$$\eta = \frac{F}{\lambda} \cdot \left(\frac{d\delta}{dt}\right)^{-1}_{constant\ load} \quad (5)$$

The average of five measurements are given in the results. Further details of the bending test analysis can be found elsewhere [4].

Additionally, indentation experiments were performed on the metallographic cross-sections of the samples. The hardness and elastic modulus of top coats were measured with a depth-sensing micro-indentation test (H-100 Fischerscope, Helmut Fischer GmbH, Sindelfingen, Germany). The load applied on the indenter was set to be 1 N. An effective Young's modulus was calculated from the initial unloading slope [19]. The elastic modulus of the materials can be obtained with the following equation:

$$E^* = \frac{E}{(1 - v^2)} \quad (6)$$

where E is the elastic modulus (GPa) of the tested material, E^* is the measured effective Young's modulus (GPa) (corrected for the stiffness of the indenter), and v is the Poisson's ratio which was taken as 0.25. A mean value of 8 to 10 indentations is shown as the result.

3. Results and Discussion

First of all, the metallographic sections of the free-standing coatings were analyzed by SEM. In Figure 2 a–d an overview of the coatings and in Figure 2 e–h higher magnifications are shown. The micrographs looked homogenous and also the high magnifications did not reveal a significant difference between the coatings. Microcracks were visible in all coatings and differences in the morphology of the cracks could not be clearly stated, at least not in a quantitative manner. As small changes in the microstructure are not visible in SEM analysis, another technique to investigate microcracks, mercury porosimetry, was applied. The higher roughness of the sample with the graphite substrate is a result of the higher roughness of this substrate, which is discussed later.

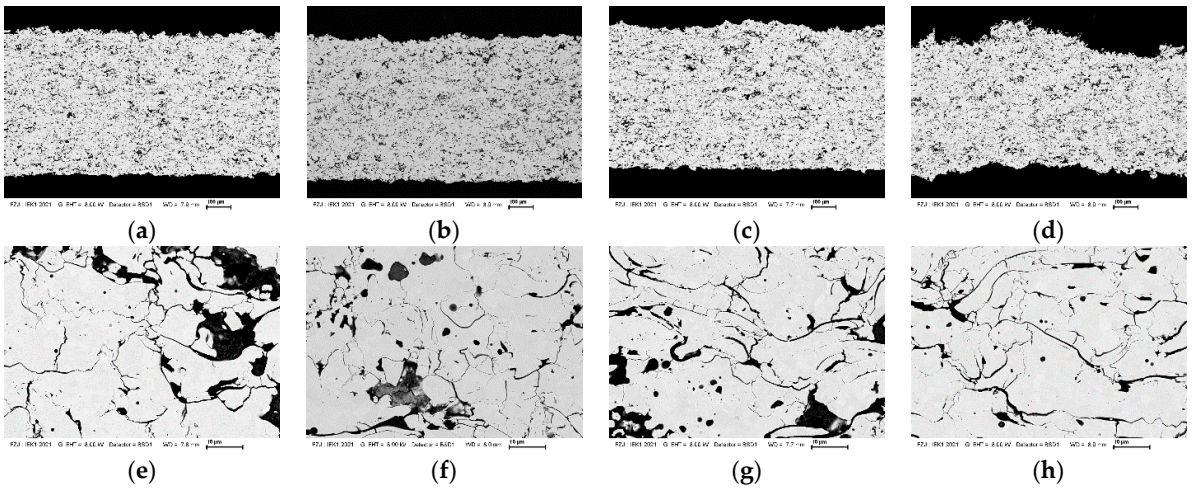

Figure 2. SEM images of the free-standing coatings with lower magnification (**a**) NaCl, (**b**) EC, (**c**) HCl, and (**d**) graphite, and higher magnification (**e**) NaCl, (**f**) EC, (**g**) HCl, and (**h**) graphite.

In Figure 3a, the results of the porosimetry measurements are shown. In this method, there might be a significant scatter between the different measurements of the same coating. Therefore, an estimation of the amount of scattering was obtained by performing two measurements (named as a and b) for each type of coating. According to the results, the difference between the two measurements was always below 1%. The lowest porosity was observed for the coating which was electrochemically removed. The next highest porosity level was measured for the NaCl and then the HCl method. The highest pore volume was detected in the coating prepared via the graphite method. This result can be explained by the higher roughness of the coating in the graphite method, which can be noticed in Figure 1 and will be further discussed below.

In order to obtain a better insight into the difference between the porosimetry measurements of the different samples, an evaluation of the change of the pore volume for a pore radius interval was made. The results are shown in Figure 3b for the pore size range in which most of the pore volume was found, i.e., between a pore radius of 100 nm and 1 μm. Due to the limited resolution, the scattering of the data was quite high although the data had already been smoothed. Despite this, a number of conclusions could be made. The maximum of the differentials was at a pore radius (r_{pore}) of about 0.5 μm for all coatings. This would indicate that the opening of the cracks should be about 1 μm, however looking at the high magnification images in Figure 1b, 1 μm appears to be too large. The overestimation of the crack opening might be due to two factors. First, the pore size calculation of the mercury porosimetry uses the Washburn equation ([20]):

$$r_{pore} = \frac{2\gamma \cos \theta}{p} \tag{7}$$

in which θ is the wetting angle, γ is the surface tension of mercury, and p is the applied pressure. As this equation is based on cylindrical pores, the geometry of cracks would reduce the pore diameter up to a factor of two. Second, the pressure necessary to fill a crack might open the crack further and by this close the finer pores. This results in an increase in the measured pore sizes, which is opposite to another more general tendency in mercury porosimetry. When large pores in the microstructure are connected to the surface only via small pores, pore size distribution tends to shift toward finer pore sizes. This is because large pores are only filled when the pressure is high enough to penetrate through the small pores. This can be found in thermally sprayed, micro-cracked ceramic coatings, i.e., the large pore volume measured using the mercury porosimetry is often rather small compared to the results obtained in image analysis. However, although there is certainly a systematic error regarding the pore size, it is expected that this is similar for all coatings detached via different methods and the results can be well compared.

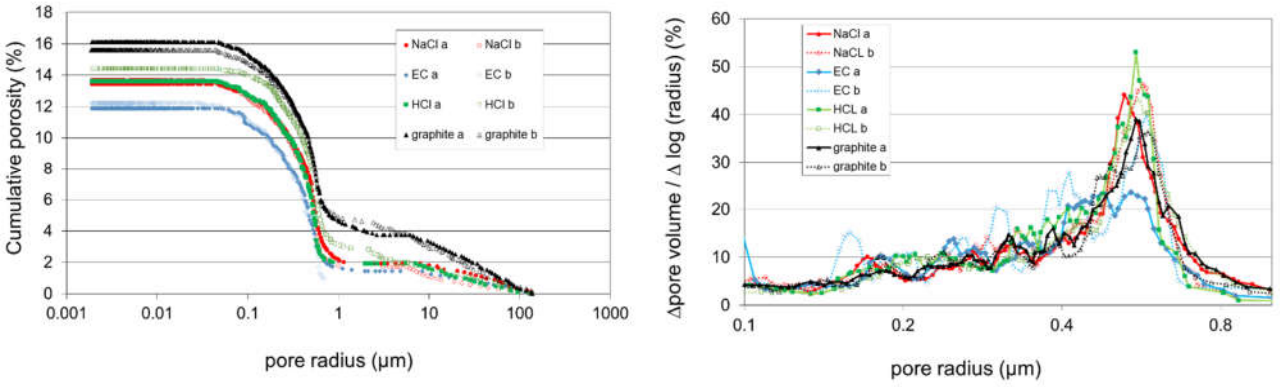

(**a**) (**b**)

Figure 3. Mercury porosimetry results. (**a**) Cumulative pore volume of the whole measurement range and (**b**) differential pore volume of the size range between 100 nm and 1 µm as a function of the pore radius (logarithmic scale).

In Figure 3b, it is visible that the average results for NaCl and HCl at the location of the maximum (r_{pore} ≈ 0.5 µm) are the highest followed by graphite and EC. In contrast, at finer pore sizes, the EC sample gives slightly higher values. Having in mind that the integral of the corresponding curves gives the pore volume, it can be concluded that some of the finer pores were coarsened probably by chemical dissolution of the YSZ in the HCl treatment [21].

The influence of the NaCl interlayer appears to be less clear. It is expected that the bonding between coating and substrate is reduced by this interlayer. As a result, a significantly reduced stress level and hence a lower amount of stress relaxation is expected which probably would lead to fewer cracks and reduced crack opening in contrast to findings shown in Figure 3. Another factor is the thermal conductivity of NaCl of about 6.2 W/m/K which is considerably lower than the one of steel. That should increase the deposition temperature and lower the stress levels during cooling and hence, reduce the cracking as well. The melting temperature of NaCI is 801 °C and it has low strength especially at elevated temperatures [22]. Additionally, it has a low modulus (below 50 GPa) and a large thermal expansion coefficient (>35 × 10^{-6}/K) [23]. All these properties lead to a rather soft substrate whereon even already deposited splats might deform to some extent by the impingement of new splats. That might lead to slightly increased crack opening as observed in Figure 3b. Similarly, graphite has limited strength and a low modulus, which could also lead to the increased crack opening in this method. Figure 4 reveals the microtopography of the top and bottom (the side in contact with the substrate) surface of different coatings. Among others, the bottom surface of the coating detached via the graphite method was more uneven with visible deep craters. This explains the increased pore volume in the graphite method (see Figure 3a) as a certain amount of pressure would be necessary to intrude the mercury into this uneven surface. This explanation was further confirmed by the higher amount of large pores in this coating, i.e., there was about 1% of additional porosity in the size range above 10 µm. It is assumed that the roughness does not have a direct effect on the coating process and hence the porosity of the bulk sample.

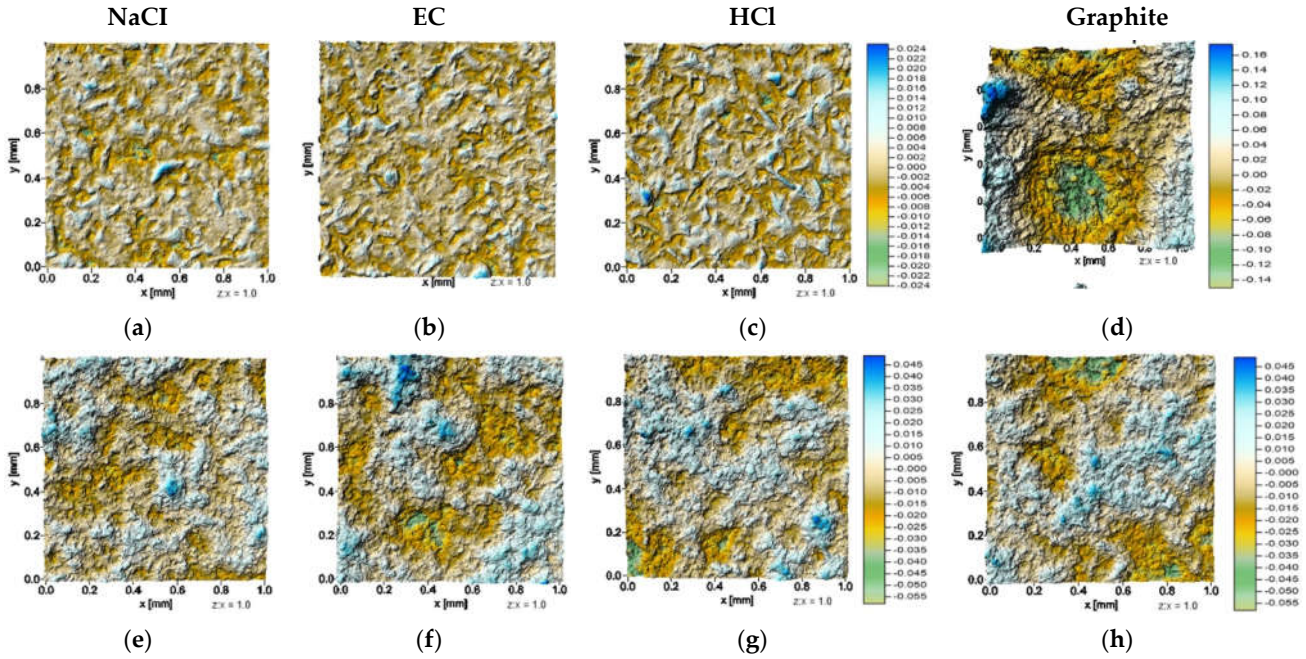

Figure 4. Microtopography of the as-sprayed, free-standing YSZ coatings. The images in the same column belong to the detachment method written on top. The top row (**a**–**d**) shows the surface of the coatings that was in contact with the substrate and the bottom row (**e**–**h**) shows the top surface of the coatings.

Figure 5 shows the roughness values R_a, R_z, and R_{max} of the as-sprayed coatings after the removal of the substrate as well as after the grinding process prior to the three-point bending test. It can be seen that the effect of the rough surface of the graphite substrate was diminished at the top surface compared to the bottom surface. Furthermore, the grinding could reduce the roughness for all coatings, however, the samples sprayed on graphite remained always rougher than the other samples. Obviously, it was not possible to remove all the extended roughness peaks of the graphite substrate by slight grinding. An interesting result was the large reduction in the roughness values of the top surface of the HCl-treated sample after grinding. Starting from roughness values which are comparable to the particle size of the spray powder (D10/D50/D90 = 21/53/95 µm), roughness values dropped significantly after grinding suggesting that parts and probably complete splats were removed by the grinding process. The HCl is expected to dissolve some of the necks between splats and hence reduce their bonding within the coating. As their bonding is reduced, the grinding might then be able to remove more easily the obstacles and features leading to a reduced roughness.

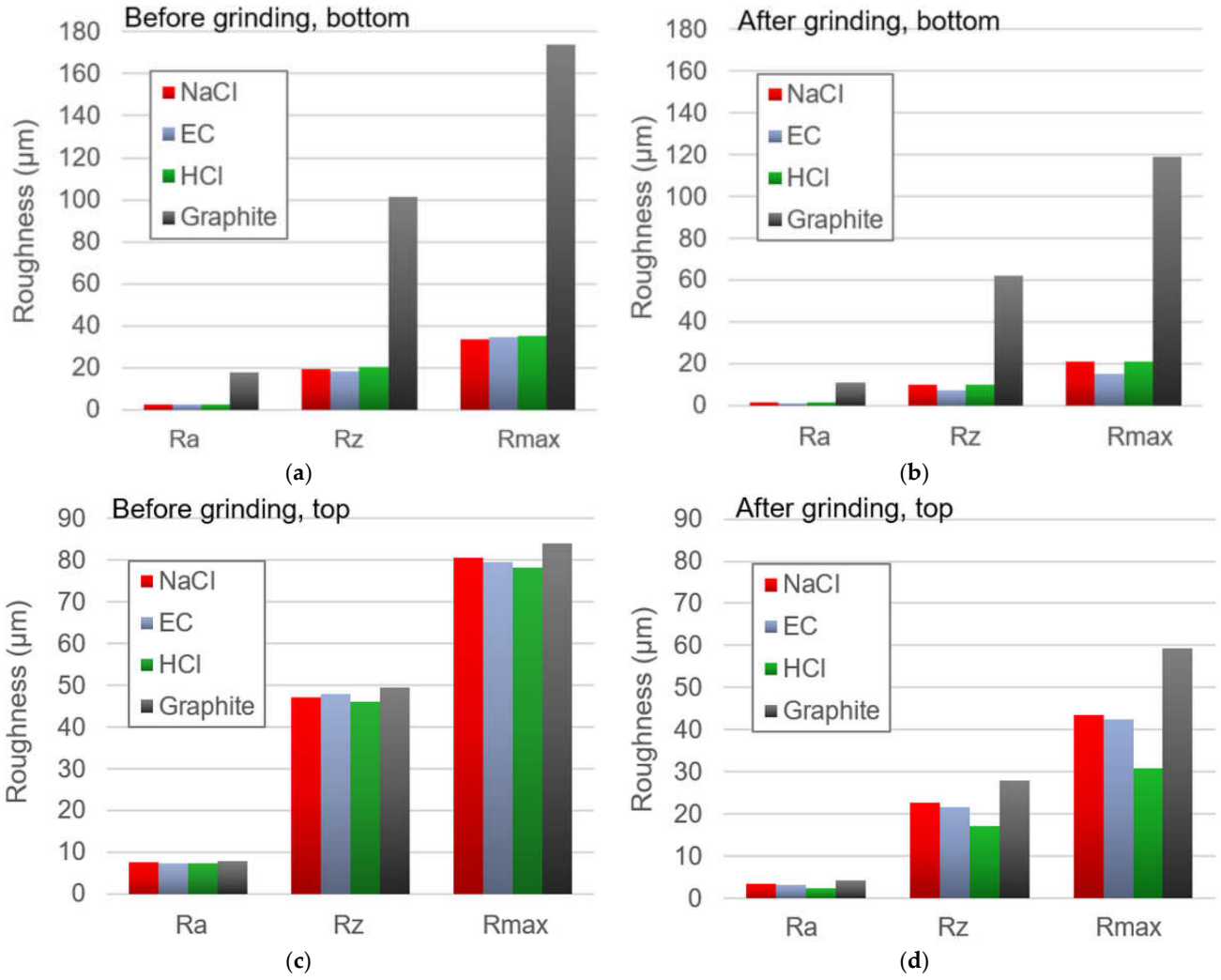

Figure 5. Roughness values of the free-standing coatings before (**a**,**c**) and after grinding (**b**,**d**). (**a**–**d**) show the roughness of the bottom surface, which was in contact with the substrate, and the top surface of the coatings, respectively.

Figure 6 shows the effect of the different removal methods on Young´s modulus of YSZ coatings as determined by three-point bending tests. In accordance with the porosimetry results (Figure 3), the EC sample with the lowest porosity showed the highest Young´s modulus. The other samples did not show too much difference in the porosity level (at least if the amount of porosity stemming from the surface roughness for the graphite sample is subtracted (~1%) or directly Figure 3b is considered). Consequently, no significant differences were observed also in Young´s modulus values. The lowest modulus was measured for the YSZ coating detached via the HCI method. This was attributed to the HCl treatment that is assumed to lead to a slight dissolution of necks between splats as discussed above. By that HCl can effectively reduce the stiffness of the porous YSZ structure resulting in a reduced modulus although the reduction of the porosity is limited.

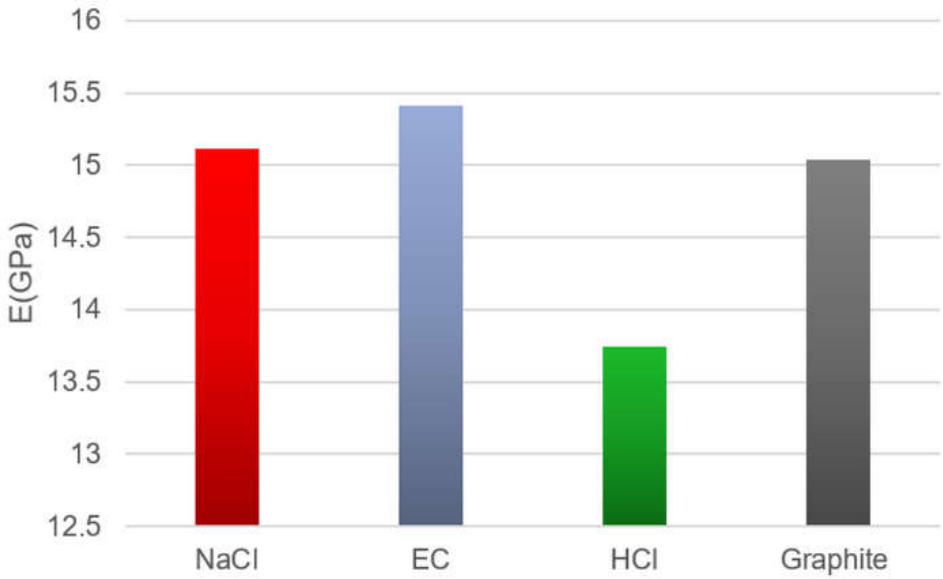

Figure 6. Young´s modulus of free-standing YSZ coatings determined by three-point bending experiments. See Table 1 for the details of different substrate removal methods.

In addition to the bending experiments, the indentation test was used to determine the Young´s modulus of YSZ coatings (Figure 7a). It is known from the literature that the localized measurement by indentation leads to considerably higher modulus values [1]. This was also clearly observed comparing Figures 6 and 7a. In addition to this finding, it was obvious that the relative behavior of the mean moduli for the different removal methods was identical to the results from the bending tests. This underlines that solid differences exist between the different removal methods. In Figure 7b the hardness results are shown. Due to the larger scattering, the comparison was not as clear as for the modulus, however, the HCl method still showed a low value compared to the EC removal method.

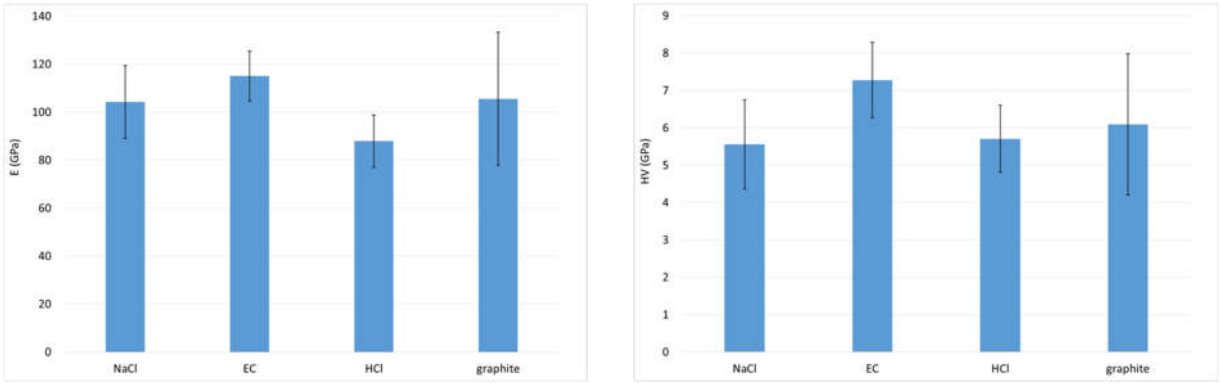

(**a**) (**b**)

Figure 7. Results of the indentation tests on free-standing YSZ coatings, (**a**) Young´s modulus, (**b**) hardness. See Table 1 for the details of different substrate removal methods.

In the bending experiment also relaxation phenomena were measured at room temperature. Clearly, a porous body with a stiff assembly of well-bonded particles (e.g., in a sintered sample) should not show such relaxation phenomena, at least not at a temperature far below the melting point as it is here in the case for YSZ (T_m~2700 °C). Earlier work showed that such room temperature relaxation processes take place in the plasma spray microstructure and the behavior cannot be extrapolated from high-temperature data, so a

different type of mechanism takes place [4]. It is assumed that the splats are able to slip along each other and by that lead to some non-elastic deformation. Determined viscosity values for all the samples are shown in Figure 8.

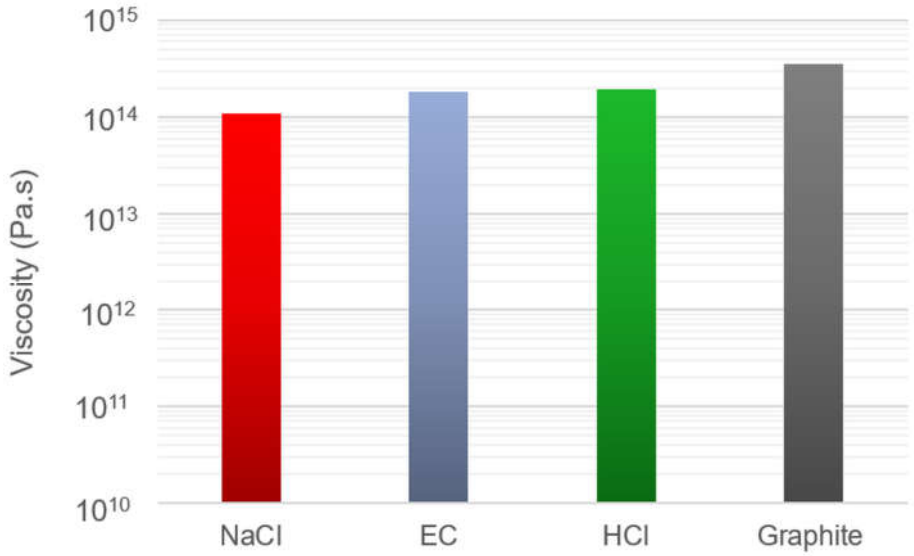

Figure 8. Viscosity of free-standing YSZ coatings determined by three-point bending experiments. See Table 1 for the details of different substrate removal methods.

The observed viscosity values are in the range between 1 and 3 × 10^{14} Pas. Whether these viscosity values (η) might lead to significant room temperature relaxation or not can be estimated by using the law for viscous flow:

$$\sigma = \eta \, \dot{\epsilon} \tag{8}$$

in which $\dot{\epsilon}$ is the strain rate and σ is the stress. Assuming a stress level of 100 MPa, a strain rate of about ~10^{-6}/s is calculated. That means, to have a total strain of about 1%, only some hours would be necessary (neglecting that the stress will reduce and hence the strain rate). Therefore it is obvious that room temperature relaxation can play a major role and it has already been introduced in a lifetime model for thermal barrier coatings [24].

Although the viscous room temperature flow was measurable in all the coatings, the absolute values of the viscosities were not clear. Certainly, a high scattering is observed for these measurements as a rather small strain change has to be evaluated over a longer time. It was expected that the coating removed with the HCl method should show low viscosity as bridges between the splats are weakened and also the surface of the splats should be smoothened leading to easier gliding. However, Figure 8 shows a mean viscosity value of 2 × 10^{14} Pas for this YSZ coating. For a better understanding of the effect of removal methods on the viscosity data, a more detailed and extensive investigation is necessary.

4. Conclusions

Four different substrate removal methods for thermally sprayed YSZ coatings, namely NaCl interlayer, HCl dissolution, graphite substrate, and electrochemical removal, were compared. The employed methods resulted in different porosity values in YSZ coatings and also variations in the Young´s moduli could be observed. It was found that HCl affects the microstructure of the YSZ coatings and leads to higher porosity and lower modulus. Also using graphite substrates and NaCl interlayer introduced increased porosity and reduced stiffness. The lowest porosity and highest modulus in the YSZ were

obtained using the electrochemical dissolution method which is based on these results the best substrate removal method among others investigated in this study.

Author Contributions: R.V. initiated the work, analyzed the data and has written the paper, E.B. made the bending experiments and contributed to the writing of the paper. S.S.-L. performed the removal and the indentation experiments and carefully read the paper. All authors have read and agreed to the published version of the manuscript.

Funding: Funding was supplied by the Helmholtz association.

Institutional Review Board Statement: Not applicable.

Informed Consent Statement: Not applicable.

Data Availability Statement: The data presented in this study are available on request from the corresponding author.

Acknowledgments The authors thank Frank Kurze, IEK-1, for the coating manufacture and Volker Bader, IEK-1, for the heat treatments. In addition, the support of Steffen Brinckmann, IEK-2, with respect to the indentation tests is acknowledged.

Conflicts of Interest: The authors declare no conflict of interest.

References

1. Basu, D.; Funke, C.; Steinbrech, R.W. Effect of heat treatment on elastic properties of separated thermal barrier coatings. *J. Mater. Res.* **1999**, *14*, 4643–4650, doi:10.1557/jmr.1999.0628.
2. Neumann, M.; Gehre, P.; Hubálková, J.; Zielke, H.; Abendroth, M.; Aneziris, C.G. Statistical Analysis of the Flexural Strength of Free-Standing Flame-Sprayed Alumina Coatings Prior and After Thermal Shock. *J. Therm. Spray Technol.* **2020**, *29*, 1–7, doi:10.1007/s11666-020-01114-6.
3. Soltani, R.; Coyle, T.W.; Mostaghimi, J. Creep Behavior of Plasma-Sprayed Zirconia Thermal Barrier Coatings. *J. Am. Ceram. Soc.* **2007**, *90*, 2873–2878, doi:10.1111/j.1551-2916.2007.01822.x.
4. Ahrens, M.; Lampenscherf, S.; Vaßen, R.; Stöver, D. Sintering and Creep Processes in Plasma-Sprayed Thermal Barrier Coatings. *J. Therm. Spray Technol.* **2004**, *13*, 432–442, doi:10.1361/10599630420434.
5. Lv, B.; Mücke, R.; Fan, X.; Wang, T.; Guillon, O.; Vaßen, R. Sintering resistance of advanced plasma-sprayed thermal barrier coatings with strain-tolerant microstructures. *J. Eur. Ceram. Soc.* **2018**, *38*, 5092–5100, doi:10.1016/j.jeurceramsoc.2018.07.013.
6. Cipitria, A.; Golosnoy, I.; Clyne, T. A sintering model for plasma-sprayed zirconia TBCs. Part I: Free-standing coatings. *Acta Mater.* **2009**, *57*, 980–992, doi:10.1016/j.actamat.2008.10.024.
7. Vaßen, R.; Czech, N.; Mallener, W.; Stamm, W.; Stöver, D. Influence of impurity content and porosity of plasma sprayed yttria stabilised zirconia layers on the sintering behaviour. *Surface Coat. Technol.* 2001, 141, 135–140.
8. Smith, G.M.; Smith, A.; Sampath, S. Fracture Toughness of Thermal Spray Ceramics: Measurement Techniques and Processing Dependence. *J. Therm. Spray Technol.* **2018**, *27*, 1076–1089, doi:10.1007/s11666-018-0755-6.
9. Neumann, M.; Gehre, P.; Kuebler, J.; Dadivanyan, N.; Jelitto, H.; Schneider, G.A.; Aneziris, C.G. Stable crack propagation in free standing thermal sprayed Al_2O_3 and $Al_2O_3ZrO_2TiO_2$ coatings. *Ceram. Int.* **2019**, *45*, 8761–8766, doi:10.1016/j.ceramint.2019.01.200.
10. Lin, C.-K.; Berndt, C.C.; Leigh, S.-H.; Murakami, K. Acoustic Emission Studies of Alumina-13% Titania Free-Standing Forms during Four-Point Bend Tests. *J. Am. Ceram. Soc.* **2005**, *80*, 2382–2394, doi:10.1111/j.1151-2916.1997.tb03130.x.
11. Sivakumar, S.; Shanmugavelayutham, G.; Yugeswaran, S.; Mostaghimi, J. Influence of water vapour on structural and thermal conductivity of post-heat treated plasma sprayed LZ and YSZ coatings. *J. Alloy. Compd.* **2018**, *740*, 212–221, doi:10.1016/j.jallcom.2018.01.056.
12. Wang, L.; Habibi, M.; Eldridge, J.I.; Guo, S. Infrared radiative properties of plasma-sprayed $BaZrO_3$ coatings. *J. Eur. Ceram. Soc.* **2014**, *34*, 3941–3949, doi:10.1016/j.jeurceramsoc.2014.05.015.
13. Lipkin, D.M.; Krogstad, J.A.; Gao, Y.; Johnson, C.A.; Nelson, W.A.; Levi, C.G. Phase Evolution upon Aging of Air-Plasma Sprayed t′-Zirconia Coatings: I—Synchrotron X-Ray Diffraction. *J. Am. Ceram. Soc.* **2013**, *96*, 290–298.
14. Li, W.; Zhao, H.; Zhong, X.; Wang, L.; Tao, S. Air Plasma-Sprayed Yttria and Yttria-Stabilized Zirconia Thermal Barrier Coatings Subjected to Calcium-Magnesium-Alumino-Silicate (CMAS). *J. Therm. Spray Technol.* **2014**, *23*, 975–983, doi:10.1007/s11666-014-0107-0.
15. Waki, H.; Nishikawa, I.; Kobayashi, A.; Ishii, N. Sensitivity to experimental errors in evaluating the thermal expansion coefficient of a thermal barrier coating by using coating system specimens. *Vacuum* **2013**, *88*, 93–97, doi:10.1016/j.vacuum.2012.03.018.
16. Wakui, T.; Malzbender, J.; Steinbrech, R. Strain dependent stiffness of plasma sprayed thermal barrier coatings. *Surf. Coatings Technol.* **2006**, *200*, 4995–5002, doi:10.1016/j.surfcoat.2005.05.001.
17. Cipitria, A.; Golosnoy, I.; Clyne, T. A sintering model for plasma-sprayed zirconia thermal barrier coatings. Part II: Coatings bonded to a rigid substrate. *Acta Mater.* **2009**, *57*, 993–1003, doi:10.1016/j.actamat.2008.10.058.
18. Lutz, E.H., Plasma Ceramics—Prperties and Applications. *cfi/Ber DKG* **1997**, *74*, 148–151.

19. Oliver, W.; Pharr, G. An improved technique for determining hardness and elastic modulus using load and displacement sensing indentation experiments. *J. Mater. Res.* **1992**, *7*, 1564–1583, doi:10.1557/jmr.1992.1564.
20. Washburn, E.W. The Dynamics of Capillary Flow. *Phys. Rev.* **1921**, *17*, 273–283, doi:10.1103/physrev.17.273.
21. Manna, M.F.; Grandstaff, D.E.; Ulmer, G.C.; Vicenzi, E. P. The chemical durability of yttria-stabilized ZrO_2 pH and O_2 geothermal sensors. *Water Rock Interact.* **2007,** *1–2,* 233-236.
22. Conrad, H.; Yang, D. The rate-controlling mechanism(s) during plastic deformation of polycrystalline NaCl at 0.28–0.75 TM. *J. Mater. Sci.* **1999**, *34*, 821–826, doi:10.1023/a:1004537300154.
23. matweb Materials Property Data. 2021. Available online: http://www.matweb.com (accessed on March 20, 2021).
24. Vaßen, R.; Giesen, S.; Stöver, D. Lifetime of Plasma-Sprayed Thermal Barrier Coatings: Comparison of Numerical and Experimental Results. *J. Therm. Spray Technol.* **2009**, *18*, 835–845, doi:10.1007/s11666-009-9389-z.